Provided for non-commercial research and education use.
Not for reproduction, distribution or commercial use.

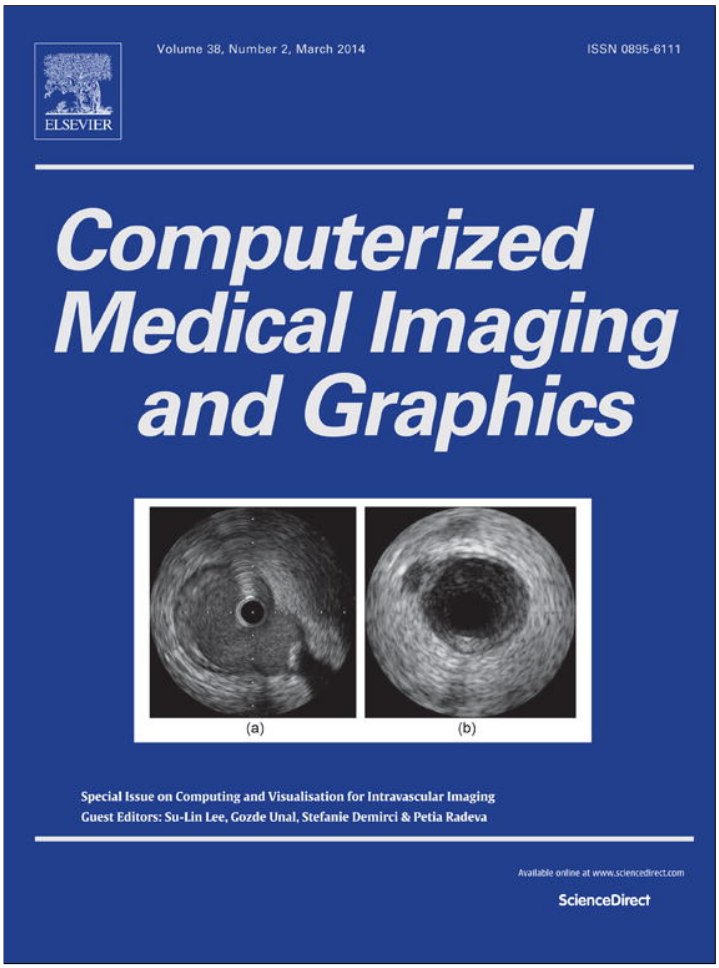

This article appeared in a journal published by Elsevier. The attached copy is furnished to the author for internal non-commercial research and education use, including for instruction at the authors institution and sharing with colleagues.

Other uses, including reproduction and distribution, or selling or licensing copies, or posting to personal, institutional or third party websites are prohibited.

In most cases authors are permitted to post their version of the article (e.g. in Word or Tex form) to their personal website or institutional repository. Authors requiring further information regarding Elsevier's archiving and manuscript policies are encouraged to visit:

http://www.elsevier.com/authorsrights

Author's personal copy

Computerized Medical Imaging and Graphics 38 (2014) 123–136

Contents lists available at ScienceDirect

Computerized Medical Imaging and Graphics

journal homepage: www.elsevier.com/locate/compmedimag

A local angle compensation method based on kinematics constraints for non-invasive vascular axial strain computations on human carotid arteries

Elizabeth Mercure[a], François Destrempes[a], Marie-Hélène Roy Cardinal[a], Jonathan Porée[a], Gilles Soulez[b], Jacques Ohayon[c,d], Guy Cloutier[a,b,*]

[a] Laboratory of Biorheology and Medical Ultrasonics, University of Montreal Hospital Research Center (CRCHUM), Montreal, Canada
[b] Department of Radiology, Radio-Oncology and Nuclear Medicine, and Institute of Biomedical Engineering, University of Montreal, Montreal, Canada
[c] Laboratory TIMC-IMAG/DyCTiM, UJF, CNRS UMR 5525, Grenoble, France
[d] University of Savoie, Polytech Annecy-Chambéry, Le Bourget du Lac, France

ARTICLE INFO

Article history:
Received 1 October 2012
Received in revised form 28 June 2013
Accepted 7 August 2013

Keywords:
Ultrasound elastography
Carotid artery
Strain tensor
Angle-dependence
Strain rate
Healthy carotids
Atherosclerotic plaques
Vulnerable carotid plaques

ABSTRACT

Non invasive vascular elastography (NIVE) was developed to highlight atherosclerotic plaque constituents. However, NIVE motion estimates are affected by artifacts, such as an underestimation of deformations due to projected movement angles with respect to the ultrasound beam, movements of the operator or of the patient during image acquisition. The main objective of this work was to propose a local angle compensation method within small measurement windows for the axial strain based on kinematics constraints, and to introduce a filtering process on the strain time-varying curve to reduce as much as possible the impact of motion artifacts. With such preprocessing, we successfully quantified the strain behavior of near and far walls in longitudinal images of internal carotid arteries without ($n=30$) and with ($n=21$) significant atherosclerotic disease (greater than 50% stenosis). Maximum strain rates of 4.49% s^{-1} for the healthy group and of 2.29% s^{-1} for the atherosclerotic group were calculated on the far wall of internal carotid arteries; significant differences were found between these values ($p=0.001$). The minimum strain rates, also on the far wall of internal carotid arteries, of −3.68% s^{-1} for the healthy group and of −1.89% s^{-1} for the atherosclerotic group were significantly different as well ($p=8\times10^{-4}$). The mean systolic, diastolic and cumulated axial strains could also distinguish the two groups after normalization by the pressure gradient between acquired images. To conclude, the proposed techniques allowed to differentiate healthy and atherosclerotic carotid arteries and may help to diagnose vulnerable plaques.

© 2013 Elsevier Ltd. All rights reserved.

1. Introduction

Stroke is the third leading cause of death and the first cause of morbidity in western countries [1]. Mainly due to atherosclerosis, 60% of all cerebral infarctions are linked to the rupture of a vulnerable plaque [2]. Carotid stenosis has long been the primary marker of vulnerability. However, it has been shown that calcified plaques are less prone to rupture than non calcified plaques [3] and are thus more stable. A vulnerable plaque can be characterized by a soft necrotic core embedded in the wall under a thin fibrous cap [4]. In fact, plaque vulnerability is multifactorial and depends mainly on its tissue composition (fibrotic, calcified and lipidic) and the biomechanical properties of its components. The studies [5,6], and later [7,8], have shown that circumferential stress, more specifically the "peak cap stress" (PCS), is a strong mechanical indicator of vulnerability. The PCS mainly depends on the fibrous cap thickness, lipid core Young modulus and blood pressure. In this context, it is relevant to assess plaque morphology, composition and biomechanical properties to prevent stroke events. Mechanical properties of the arterial wall have been the subject of numerous researches and various tools have been developed using ultrasound imaging to measure compliance, distensibility, stiffness [9–12], and elasticity [13–17].

Elastography is an ultrasound imaging technique for estimating elastic properties of tissues [18]. It has been extensively studied for the diagnosis of breast, liver, prostate and thyroid [17]. In the context of diagnosis of arterial vascular diseases, the pioneer work in intravascular elastography by [19–22] using intravascular ultrasound (IVUS) catheter has shown the ability to distinguish between fiber, fibro fatty and fatty plaque components based on the radial

* Corresponding author at: Laboratory of Biorheology and Medical Ultrasonics, University of Montreal Hospital Research Center (CRCHUM), Montreal, Canada. Tel.: +1 514 890 8000x24703; fax: +1 514 412 7505.
E-mail address: guy.cloutier@umontreal.ca (G. Cloutier).

0895-6111/$ – see front matter © 2013 Elsevier Ltd. All rights reserved.
http://dx.doi.org/10.1016/j.compmedimag.2013.08.005

Author's personal copy

strain. Later, different components of the full strain tensor were proposed and studied [23–32] in the context of human coronary and carotid arteries. More recently, IVUS elastography has led to a promising tool known as modulography [13,16,33–38], which aims at computing the Young modulus mapping of the arterial wall. Although IVUS imaging provides a higher spatial resolution than external echography, the main modality used for superficial vessels, such as the carotid artery, is external echography due to its non-invasiveness. Elastography studies have been performed on human carotid arteries using cross-correlation algorithms [39–42] and the Lagrangian speckle model estimator (LSME) [43–46], which allows the computation of the complete 2D strain tensor. Thus, the LSME gives access from a single optimization to axial and lateral strains and shears. These studies have shown a potential for non-invasive vascular elastography (NIVE) to evaluate arterial stiffness and plaque morphology based on strain and shear maps. In both IVUS and NIVE elastography, the natural pulsation of the blood flow induces vessel motion and deformation, which are detected by ultrasound speckle tracking applied on either B-mode or radio-frequency (RF)-mode data.

Noninvasive vascular imaging techniques still present challenges. Due to the low lateral resolution of external echography using standard beamforming, the lateral components of the displacement gradient matrix are less reliable than the axial ones [47–49], thus limiting the evaluation of the strain tensor to the axial strain and shear components. In this context, one would prefer a longitudinal analysis of the artery to a cross-sectional one, since displacements and deformations will then mainly occur in the axial direction. Moreover, it has been shown, with IVUS elastography [50,51] and NIVE [52], that the strain tensor depends on the coordinate system and needs to be corrected for a reliable interpretation. In IVUS, due to the catheter eccentricity, the strain tensor needs to be transformed towards the vessel coordinate system. Similarly, in external elastography, the strain tensor can be compensated for the local wall deformation direction.

The first goal of this paper is to provide a new local compensation method based on the plane strain condition in the context of NIVE. Previous angle correction methods for the strain estimate were presented to obtain a compounded strain image or to determine the normal strain tensor, in the context of beam-steered data [53–57]. However, the beam-steering approaches consider angles (for each direction of the beam-steering) that are global to the image. As far as we know, this is a difference with our proposed angle compensation method, where the angle is computed locally on measurement windows. The effect of the angle compensation on the axial strain time-varying curves was also investigated. Moreover, the resulting temporal strain rate evolution – a parameter that was previously described for cardiac strain application [58–64] – is presented and discussed in this work. In order to compute the strain rate, a filtering method that keeps the principal frequency components close to the heartbeat frequency is introduced. It is shown that the strain rate computed on the filtered axial strain curves is able to differentiate normal from atherosclerotic carotid walls, with or without the angle compensation.

2. Materials and methods

With the database described next, we propose pre-processing steps to optimize the reliability of axial strain estimates. The scheme first requires an initialization followed by an automatic segmentation of all frames of a video RF-mode sequence of the carotid artery; the computation of the elastogram within the segmented region of all frames; the determination of the time-varying mean strains within the segmented region; the angle compensation of mean strain values; the bandpass filtering of time-varying mean strain curves; and the extraction of quantitative structural parameters for diagnostic purpose. These pre-processing steps are described below.

2.1. Recruitment of participants

All subjects signed a written informed consent form approved by the ethical committee of the University of Montreal Hospital Research Center. Fifteen healthy subjects had no sign of carotid plaque and they had no history of cardiovascular or cerebrovascular diseases. Seven women and eight men, ranging in age from 41 to 71 years, constituted the healthy group. The atherosclerotic group diagnosed with a carotid stenosis of at least 50% in diameter reduction was composed of 4 women and 17 men, for a total of 21 patients, aging from 56 to 80 years old. Since one of the objectives of this study was to propose a compensation method to correct axial strain distributions for both near and far walls,[1] we have only selected patients for which one of the internal carotid arteries exhibited a plaque on both near and far walls of the vessel.

2.2. Data acquisition

To identify the carotid plaque, the first step of the acquisition process consisted of a conventional duplex B-mode and echo Doppler examination with a Philips 5000 system (Philips Medical Systems, Bothell, WA, USA). As shown in Fig. 1, Doppler scan helps locating hypoechoic plaques, which can be difficult to see in conventional B-mode examination. Next, RF data were recorded with a Sonix RP scanner (Ultrasonix, Vancouver, BC, Canada) using a 10 MHz frequency transducer (model L14-5/38, 128 elements, 7.2 MHz center frequency with a fractional bandwidth of 70% at −6 dB) with a sampling frequency of 40 MHz. The nominal center frequency was around 5.2 MHz on the RF data due to the high-frequency tissue attenuation. The RF acquisition frame rate varied from 16 to 42 images per second according to the depth of field of the RF images (based on the location of the wall or plaque). For the 15 subjects with healthy carotids, both carotids were imaged (left and right). For the 21 patients, the image was acquired on the side of the plaque.

2.3. Image segmentation

Longitudinal image sequences of a few seconds of the internal carotid artery were segmented using semi-automatic methods described elsewhere [65,66]. Healthy subject sequences were treated with the algorithm described in [65]. This algorithm performs the segmentation of the intima-media thickness (IMT) using prior knowledge on the size of the human IMT and a likelihood based on mixtures of Nakagami distributions used to describe first order statistics of the RF echo envelope. In this context, the IMT refers to the intima-media complex, with boundaries made of the lumen-intima and media-adventitia interfaces. The statistical parameters of the mixtures of Nakagami distributions were estimated using an Expectation-Maximization algorithm [67]. The segmentation of the IMT (for healthy vessel walls) is viewed as the maximum a posteriori (MAP) of a Bayesian model, which was computed with a stochastic optimization algorithm. This semi-automatic segmentation method requires a user to manually select 3–5 points within the IMT on a single (arbitrary) reference frame. It was demonstrated in [65] on a database of 30 sequences of ultrasonic B-mode images of presumably disease-free control subjects

[1] Near and far walls of the carotid artery are defined with respect to the probe position.

Author's personal copy

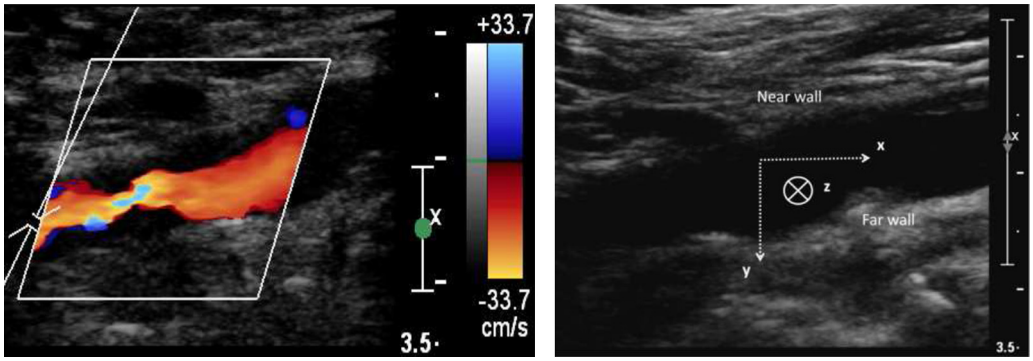

Fig. 1. Longitudinal color-Doppler image of the right proximal internal carotid artery of a patient acquired with the Philips 5000 ultrasound system (left) and its corresponding B-mode image (right). The maximal depth of each image is 3.5 cm and the distance between the scale graduation marks is 1 cm.

that the segmentation method was within the variability of the manual segmentations by two experts.

Atherosclerotic group sequences were segmented using another method described in [66]. As the previous one, it takes a manual segmentation in a reference frame as input, refines that segmentation, and tracks this region over the whole video sequence. The prior of the underlying Bayesian model of this algorithm is based on motion field estimation and is used as a spatio temporal constraint. As carotid plaques are usually more heterogeneous, the likelihood based on mixtures of Nakagami distributions is particularly convenient here. It was shown in [66] on a database of 94 sequences of 33 patients that the segmentation algorithm was not sensitive to the degree of stenosis or calcification present in the plaque. Moreover, paired t-tests with a confidence level of 0.05 showed that there were no significant difference in the semi-automatic segmentations with or without random perturbation of the manual initializations of the reference frame within a distance of 0.5 mm. Thus, the segmentation method is robust to a certain lack of precision in the manual initialization of the segmentations of the reference frame.

In both cases, plaques and normal walls were segmented in the reference frame of the sequence by a technician. Both near and far walls of the vessel were segmented separately. All segmentations were validated by a radiologist (G.S.).

2.4. Elastogram computation

Elastograms were computed using the LSME previously developed in [43,68,69]. This algorithm allows the estimation of the four components of the 2D displacement gradient matrix in the image plane, from which the strain components are deduced (axial and lateral strains and shears). The computations are performed on small regions-of-interest (ROIs) also called measurement windows. The first step of this implementation compensates for the translation motion of the ROI, using a cross-correlation method. In the second step, the displacement gradient matrix is computed by solving an extended version of the optical flow equation [69], in which the displacement field is assumed to be linear in the ROI and is approximated by its first order Taylor expansion. This second step provides a sub-pixel translation, as well as the four components of the 2D displacement gradient matrix.

For all healthy and atherosclerotic subjects, each measurement window was set to 1.540 mm axially $\times$ 3.125 mm laterally, with 94% axial and 90% lateral overlaps as in [44,45,52]. The choice adopted in these references was an empirical tradeoff between sensitivity and resolution: the better the sensitivity, the lower the resolution of the elastogram. As for the overlapping of the ROIs, since a healthy IMT is typically less than 1 mm thick [4], a high axial and lateral overlap is necessary to obtain a significant number of points in the elastograms. The lateral overlap allows spatial smoothing along the artery wall in longitudinal views. To avoid spurious estimates of the displacement gradients due to the blood flow, each measurement window was clipped to remove the lumen area, thus limiting estimates to vessel wall tissue deformations. Any given elastogram within a cardiac cycle was computed from pair of consecutive images in the RF sequence. All elastograms were post-processed using a 5×5 pixel median filter to remove potential outliers.

More details are now given. In the sequel, the longitudinal image plane is represented by the (x, y)-plane and the z-axis denotes the axis perpendicular to that plane; see Figs. 1 and 2. The x-axis is chosen so that it is perpendicular to the ultrasound beam. Next, one considers the displacement field in the form $\vec{U} = (U_x, U_y, U_z)$ corresponding to the motion and deformation of the arterial wall under the intraluminal pressure in a small ROI. Namely, one assumes the model $\vec{x}_t = \vec{x}_{t-1} + \vec{U}(\vec{x}_{t-1})$, where $\vec{x}_{t-1}$ and $\vec{x}_t$ are the positions of a same material point in the ROI at two instants $t-1$ and t corresponding to two consecutive frames (see [69]). Adopting a first-order approximation of the displacement field in the ROI, one writes $\vec{U}(\vec{x}_{t-1}) = \vec{\tau} + \Delta\vec{x}_{t-1}$, where $\vec{\tau}$ is a constant vector depending only on the ROI center and Δ denotes the material displacement gradient matrix estimated at the center of the ROI:

$$\begin{pmatrix} \Delta_{xx} & \Delta_{xy} & \Delta_{xz} \\ \Delta_{yx} & \Delta_{yy} & \Delta_{yz} \\ \Delta_{zx} & \Delta_{zy} & \Delta_{zz} \end{pmatrix} := \begin{pmatrix} \frac{\partial U_x}{\partial x} & \frac{\partial U_x}{\partial y} & \frac{\partial U_x}{\partial z} \\ \frac{\partial U_y}{\partial x} & \frac{\partial U_y}{\partial y} & \frac{\partial U_y}{\partial z} \\ \frac{\partial U_z}{\partial x} & \frac{\partial U_z}{\partial y} & \frac{\partial U_z}{\partial z} \end{pmatrix}. \quad (1)$$

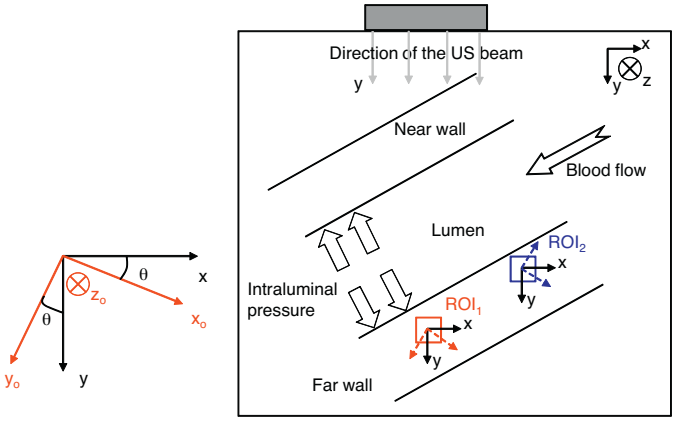

Fig. 2. Illustration of the image coordinate (x, y, z)-system related to the ultrasound (US) beam direction and the local (x_0, y_0, z_0)-system, for which the plane strain condition in the (y_0, z_0)-plane holds. The local angle θ, which depends on the region-of-interest (ROI), represents the angle between the y and y_0-axes.

Author's personal copy

Next, as in [43,68], the strain tensor ε is approximated by the symmetric real-valued matrix

$$\begin{pmatrix} \varepsilon_{xx} & \varepsilon_{xy} & \varepsilon_{xz} \\ \varepsilon_{xy} & \varepsilon_{yy} & \varepsilon_{yz} \\ \varepsilon_{xz} & \varepsilon_{yz} & \varepsilon_{zz} \end{pmatrix} \approx \frac{1}{2}(\Delta + \Delta^T). \quad (2)$$

Restricting the strain tensor ε to the longitudinal image plane, one obtains $\begin{pmatrix} \varepsilon_{xx} & \varepsilon_{xy} \\ \varepsilon_{xy} & \varepsilon_{yy} \end{pmatrix}$, where $\varepsilon_{xx} = \Delta_{xx}$ and $\varepsilon_{yy} = \Delta_{yy}$ are the axial and lateral strains, respectively, $\varepsilon_{xy} = (\Delta_{xy} + \Delta_{yx})/2$ is the shear strain, and Δ_{xy} and Δ_{yx} are called the lateral and axial shear strains, respectively.

The 2D displacement gradient matrix $\Delta_{2D} = \begin{pmatrix} \Delta_{xx} & \Delta_{xy} \\ \Delta_{yx} & \Delta_{yy} \end{pmatrix}$ is estimated from the corresponding 2D displacement model $\vec{U}_{2D}(\vec{x}_{t-1}) = \vec{\tau}_{2D} + \Delta_{2D}\vec{x}_{t-1}$. The translation vector is first roughly estimated by a vector τ_1 using a cross-correlation method that compares the given measurement window with the surrounding ones. Let $I_{t-1}(x, y)$ be the pre-motion image in the measurement window and let $I_{t-1}^{\tau_1}(x, y)$ be the pre-motion image translated by the vector τ_1. Then, one considers the vector τ_2 and the 2×2 matrix Δ_{2D} that is a solution to the nonlinear minimization problem $\min_{\tau_2,\Delta} ||I_{t-1}^{\tau_1}(x, y) - I_{Lag}(x, y)||^2$. Here, I_{Lag} is the post-motion image $I_t(x, y)$ compensated for tissue motion and deformation by τ_2 and Δ_{2D} [43,68]. Thus, although the matrix Δ_{2D} can be interpreted in terms of the displacement gradients, it is actually computed using optical flow, as proposed in [69]. The translation vector τ_1 takes care of a large displacement, whereas the vector τ_2 refines it. Altogether, the translation vector is the sum $\tau_{2D} = \tau_1 + \tau_2$ and the matrix Δ_{2D} yields the axial and lateral strains, as well as the shears.

2.5. Strain curve calculation and cardiac cycle detection

Each axial strain computed within all measurement windows of the segmented area of the carotid wall (normal wall or plaque) was spatially averaged over the whole near and far walls separately. The mean value of each elastogram of the sequence was plotted to obtain one strain curve over time for each wall of the carotid. This instantaneous axial strain curve was used to detect the systolic and diastolic phases. To validate the localization of systolic and diastolic phases on the strain curves, the M-mode image was reconstructed from RF time-varying images, showing the motion of the selected wall over time. The time-varying plots normally followed the cardiac cycle periodicity. Strain curves were also computed using the axial strain component after compensation for the angle to insure the plane strain condition, as described in Section 2.6. Moreover, the strain curves were filtered to compute the strain rate and other strain parameters (Section 2.8), using the procedure described in Section 2.7. However, only the unfiltered instantaneous axial strain curve and the M-mode were used for the localization of systolic and diastolic phases.

2.6. Angle-dependence compensation

The axial strain component in NIVE is evaluated along the ultrasound beam direction of propagation since measurement windows coincide with the (x, y) coordinate system defined earlier. If the arterial wall motion is not perfectly aligned with the ultrasound field, a bias[2] is introduced in the strain estimation [52,58]. In addition, because of the heterogeneity of the vascular tissue, mechanical interaction between tissue components may further change locally the tissue principal motion orientation. Those local changes in orientation may occur when, for example, a calcified nodule interacts with a soft lipid pool in a pulsating atherosclerotic plaque. If a plaque component occupies a given measurement window, the LSME implementation can determine locally this orientation relative to the ultrasound beam.

Recall from Section 2.4 that the longitudinal image plane is represented by the (x, y)-plane, with the x-axis perpendicular to the ultrasound beam, and that the z-axis denotes the axis perpendicular to that plane. The goal of the proposed angle-compensation method is to determine locally on each ROI the orthogonal coordinate system (x_0, y_0, z_0) for which a plane strain condition occurs in the (y_0, z_0)-plane. The following hypothesis was adopted, based on the geometry of the longitudinal image acquisition:

(H1) The x_0 and y_0-axes and the artery longitudinal axis are in the image (x, y)-plane.

From hypothesis (H1), the (x_0, y_0)-plane coincides with the (x, y)-plane. Therefore, the z and z_0-axes coincide also. Hence, it follows that the two reference systems (x, y, z) (the image reference system) and (x_0, y_0, z_0) are related by a rotation with angle θ around the z-axis; see Fig. 2. Thus, θ represents the angle between the y_0-axis and the direction parallel to the ultrasound beam in the image plane (i.e., the y-axis).

Let $\vec{U} = (U_x, U_y, U_z)$ be the displacement field corresponding to the motion and deformation of the arterial wall under the intraluminal pressure and flow in a small ROI (see Section 2.4). Let Δ be the displacement gradient matrix of Eq. (1) and ε be the corresponding strain tensor matrix as in Eq. (2). Corresponding to the two reference systems, we write Δ^0 or Δ^θ in the (x_0, y_0, z_0) reference system and the image (x, y, z) reference system, respectively. A similar notation was adopted for the displacement field and the strain tensor.

The plane strain condition in the (y_0, z_0)-plane is now expressed by making the two following hypotheses on the deformation of the arterial wall:

(H2) The displacement component $U_x^0 \equiv$ constant within a small ROI, which means that the deformation of the tissue occurs only within the cross sectional (y_0, z_0)-plane.
(H3) The displacement components U_y^0 and U_z^0 are homogeneous along the x_0-axis within the ROI, i.e. they do not depend on the coordinate x_0.

Hypothesis (H2) and the definition of Eq. (1) implies that $\Delta_{xx}^0 = \Delta_{xy}^0 = \Delta_{xz}^0 = 0$, whereas hypothesis (H3) implies that $\Delta_{yx}^0 = \Delta_{zx}^0 = 0$. From there, it follows that the strain tensor in the (x_0, y_0, z_0) reference system satisfies the identities: $\varepsilon_{xx}^0 = \varepsilon_{xy}^0 = \varepsilon_{xz}^0 = 0$. Let ε^θ be the strain tensor in the image reference system. Then, assumption (H1) yields the relation:

$$\begin{pmatrix} \varepsilon_{xx}^\theta & \varepsilon_{xy}^\theta & \varepsilon_{xz}^\theta \\ \varepsilon_{xy}^\theta & \varepsilon_{yy}^\theta & \varepsilon_{yz}^\theta \\ \varepsilon_{xz}^\theta & \varepsilon_{yz}^\theta & \varepsilon_{zz}^\theta \end{pmatrix} = \begin{pmatrix} \cos\theta & -\sin\theta & 0 \\ \sin\theta & \cos\theta & 0 \\ 0 & 0 & 1 \end{pmatrix} \begin{pmatrix} 0 & 0 & 0 \\ 0 & \varepsilon_{yy}^0 & \varepsilon_{yz}^0 \\ 0 & \varepsilon_{yz}^0 & \varepsilon_{zz}^0 \end{pmatrix} \begin{pmatrix} \cos\theta & \sin\theta & 0 \\ -\sin\theta & \cos\theta & 0 \\ 0 & 0 & 1 \end{pmatrix} = \begin{pmatrix} \sin^2\theta\ \varepsilon_{yy}^0 & -\sin\theta\cos\theta\ \varepsilon_{yy}^0 & -\sin\theta\ \varepsilon_{yz}^0 \\ -\sin\theta\cos\theta\ \varepsilon_{yy}^0 & \cos^2\theta\ \varepsilon_{yy}^0 & \cos\theta\ \varepsilon_{yz}^0 \\ -\sin\theta\ \varepsilon_{yz}^0 & \cos\theta\ \varepsilon_{yz}^0 & \varepsilon_{zz}^0 \end{pmatrix}. \quad (3)$$

[2] See Eq. (8) for a mathematical expression of that bias.

Author's personal copy

One then obtains from Eq. (3) the following relation in the longitudinal 2D image plane:

$$\begin{pmatrix} \varepsilon_{xx}^{\theta} & \varepsilon_{xy}^{\theta} \\ \varepsilon_{xy}^{\theta} & \varepsilon_{yy}^{\theta} \end{pmatrix} = \begin{pmatrix} \sin^2\theta\ \varepsilon_{yy}^{0} & -\sin\theta\cos\theta\ \varepsilon_{yy}^{0} \\ -\sin\theta\cos\theta\ \varepsilon_{yy}^{0} & \cos^2\theta\ \varepsilon_{yy}^{0} \end{pmatrix} \tag{4}$$

$$= \begin{pmatrix} \cos\theta & -\sin\theta \\ \sin\theta & \cos\theta \end{pmatrix} \begin{pmatrix} 0 & 0 \\ 0 & \varepsilon_{yy}^{0} \end{pmatrix} \begin{pmatrix} \cos\theta & \sin\theta \\ -\sin\theta & \cos\theta \end{pmatrix}. \tag{5}$$

The axial strain in the direction y_0 ($\varepsilon_{yy}^{0} = \Delta_{yy}^{0}$) is thus the deformation in the image plane that satisfies the plane strain condition and is related to the estimated axial strain ($\varepsilon_{yy}^{\theta} = \Delta_{yy}^{\theta}$) in the ultrasound beam direction and the angle θ by the following expression:

$$\varepsilon_{yy}^{0} = \frac{\varepsilon_{yy}^{\theta}}{\cos^2\theta}. \tag{6}$$

Using Eq. (4), one can also deduce the value of the angle θ:

$$\tan\theta = \frac{\sin\theta}{\cos\theta} = -\frac{-\sin\theta\cos\theta\,\varepsilon_{yy}^{0}}{\cos^2\theta\,\varepsilon_{yy}^{0}} = -\frac{\varepsilon_{xy}^{\theta}}{\varepsilon_{yy}^{\theta}}. \tag{7}$$

As was already presented in [52], there is an underestimation of the axial strain when the angle θ is non-zero and the underestimation increases with the magnitude of the angle. Eq. (6) explains this relation by showing the effect of the rotation by an angle θ on the axial strain. Thus, viewing the aligned axial strain ε_{yy}^{0} as the quantity to estimate, one obtains a bias $\varepsilon_{yy}^{\theta} - \varepsilon_{yy}^{0}$ equal to

$$(1 - \cos^2\theta)\varepsilon_{yy}^{0} \tag{8}$$

on that quantity when its estimation is based directly on the non-compensated axial strain $\varepsilon_{yy}^{\theta}$. Note that the incompressibility condition imposes that $\varepsilon_{zz}^{0} = -\varepsilon_{yy}^{0}$.

In summary, the proposed angle compensation consists of the following steps:

(1) Let Δ_{xy}^{θ}, Δ_{yx}^{θ} and Δ_{yy}^{θ} be evaluated in the small ROI as in Section 2.4 (the image plane is the (x, y)-plane and the x-axis is chosen perpendicular to the ultrasound beam). Set $\varepsilon_{yy}^{\theta} = \Delta_{yy}^{\theta}$ and $\varepsilon_{xy}^{\theta} = (\Delta_{xy}^{\theta} + \Delta_{yx}^{\theta})/2$.
(2) Compute θ based on Eq. (7).
(3) Compute the estimated value of ε_{yy}^{0} based on Eq. (6). This is the axial strain in the direction of the y_0-axis (corresponding to the plane strain condition).

Note that these angle-compensation steps are applied on each measurement window. In our implementation, a Gaussian filter was used on the angle map to impose a spatial coherence on the compensation angles. In the reported tests, the lateral and axial standard-deviations of that filter in the frequency domain were equal to 3 divided by the lateral or axial dimensions of the whole ultrasound image, respectively.

2.7. Filtering of the strain curve

Movement of the operator or of the patient during the RF image acquisition can cause artifacts in the instantaneous strain curve. To remove as much as possible those artifacts for the estimation of the strain rates, a filter was applied in the spectral domain. First, the main frequency component of the spectrogram of the time-varying instantaneous axial strains, corresponding to the heart rate of the subject, was detected. Secondly, a bandpass filter was designed using a Hanning window with upper and lower cut-off frequencies. In order to eliminate possible motion associated with breathing, and knowing that the normal human respiratory cadence is between 14 and 20 breaths per minute [70], the lower cutoff frequency was set to 0.33 Hz (20 breaths per minute). The upper cutoff frequency was chosen equal to two times the main frequency component of the spectrogram so that all harmonic frequencies were removed. Finally, the original strain curve was simply convolved with this bandpass filter. Note that the filtering process is subject dependent but is automatically implemented. In that process, the lower cutoff frequency is fixed. The upper cut-off frequency is subject dependent (because the main frequency is close to the heartbeat frequency), but is automatically estimated for each sequence. Since the applied filter is bandpass, high frequencies are removed so that the filtering process may remove details from the time-varying strain curve.

2.8. Quantitative extraction of strain parameters

The strain rate has already been used to describe myocardial function [58,64]. It quantifies the speed of deformation of a given structure. In our study, it is defined as the speed of deformation of the arterial wall during the cardiac cycle. It was obtained as the derivative of the instantaneous filtered strain curve as a function of time.

As mentioned in Section 2.5, the localization of the systolic and diastolic phases were done with the M-mode and the instantaneous unfiltered axial strain curves. Then, from the filtered instantaneous axial strain curves, two strain parameters were extracted. The mean systolic axial strain (MSAS) and mean diastolic axial strain (MDAS) represent the mean value, from all cardiac cycles available for a given subject, of systolic and diastolic peaks, respectively. The sum of each instantaneous strain value gives the cumulated time-varying strain curve. To prevent error accumulation over time, the cumulated strain curve is computed on each cardiac cycle from the instantaneous strain curve minus its average over the cycle (so, the cumulated strain curve has a value of 0 at the end of each cycle). The difference between the maximum and minimum peaks of each cycle of the cumulated curve was averaged to obtain the cumulated axial strain (CAS). See [42] for cumulated axial strain curves. Two mean values, the maximum strain rate (MaSR) and minimum strain rate (MiSR), were also extracted from the strain rate curve by taking the mean, from all cardiac cycles, of the maximum and minimum strain rate peaks. Illustration of these parameters are given in Section 3. See [58–63] for cardiac strain applications based on strain rates.

In order to take into account the variation in the frame rate, heart rate and pressure pulse, these three quantities were combined as in [45, p. 3439, Eq. (1)] to produce the pressure gradient denoted ΔP. The strain parameters MSAS, MDAS and CAS were then normalized by the pressure gradient. In the sequel, these parameters are not normalized by the pressure gradient unless otherwise stated.

3. Results

3.1. Image segmentation

Fig. 3 shows typical examples of a segmented IMT (Fig. 3 left) and carotid plaque (Fig. 3 right). To illustrate the fact that plaques have a more variable shape (in a 2D image) than healthy IMTs, we considered the coefficient of variation (standard deviation over mean value, expressed with no units) of the axial width (CVAW) over the segmented region (plaque or IMT) for each frame of the sequences. For a given sequence, the CVAW was averaged over all frames of the sequence. The CVAW of the segmented IMT on the near walls in the case of healthy carotids was 0.16 ± 0.067 ($n = 30$), whereas it was 0.17 ± 0.056 ($n = 30$) for the far walls. There was no statistically significant difference between these two values ($p = 0.573$). For the segmented plaques, the CVAW was equal to 0.42 ± 0.14 ($n = 21$)

Author's personal copy

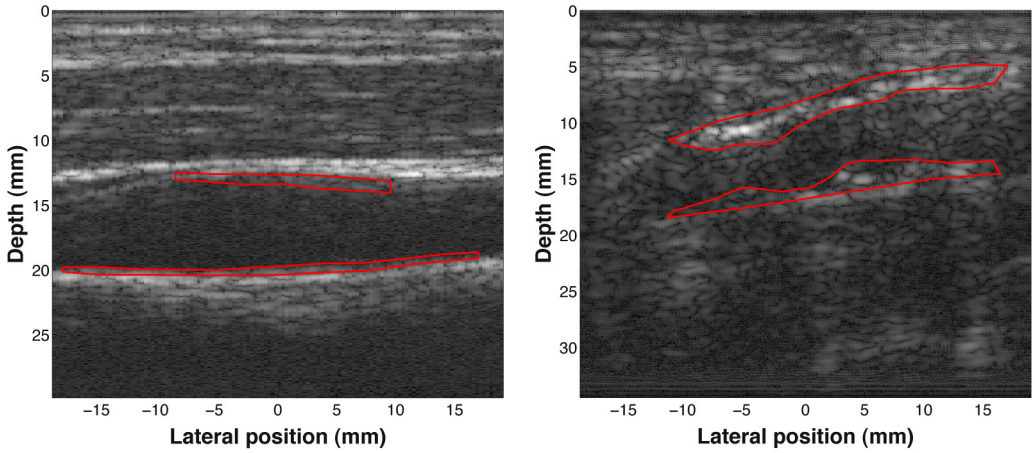

Fig. 3. Healthy intima-media thickness (IMT) segmented using the algorithm described in [65] (left) and an atherosclerotic plaque segmented using the method of [66] (right), in the reference frame of the respective sequences. Note that the clinician chose the portions of the IMT or plaque in the reference frame of each sequence to be segmented that were clearly identifiable.

for the near walls and 0.44 ± 0.095 ($n = 21$) for the far walls, again with no significant difference between the two values ($p = 0.482$). As expected, the CVAW for plaques was significantly larger than for the IMTs of healthy carotids for either walls. The statistical tests performed were t-tests with a confidence level $\alpha = 0.05$. The segmented IMTs in the case of healthy carotids had an average thickness of 0.85 ± 0.16 mm on the near walls and 0.71 ± 0.17 mm on the far walls ($n = 30$). The segmented plaques had an average thickness of 6.35 ± 2.96 mm on the near walls and 6.39 ± 2.50 mm on the far walls ($n = 21$).

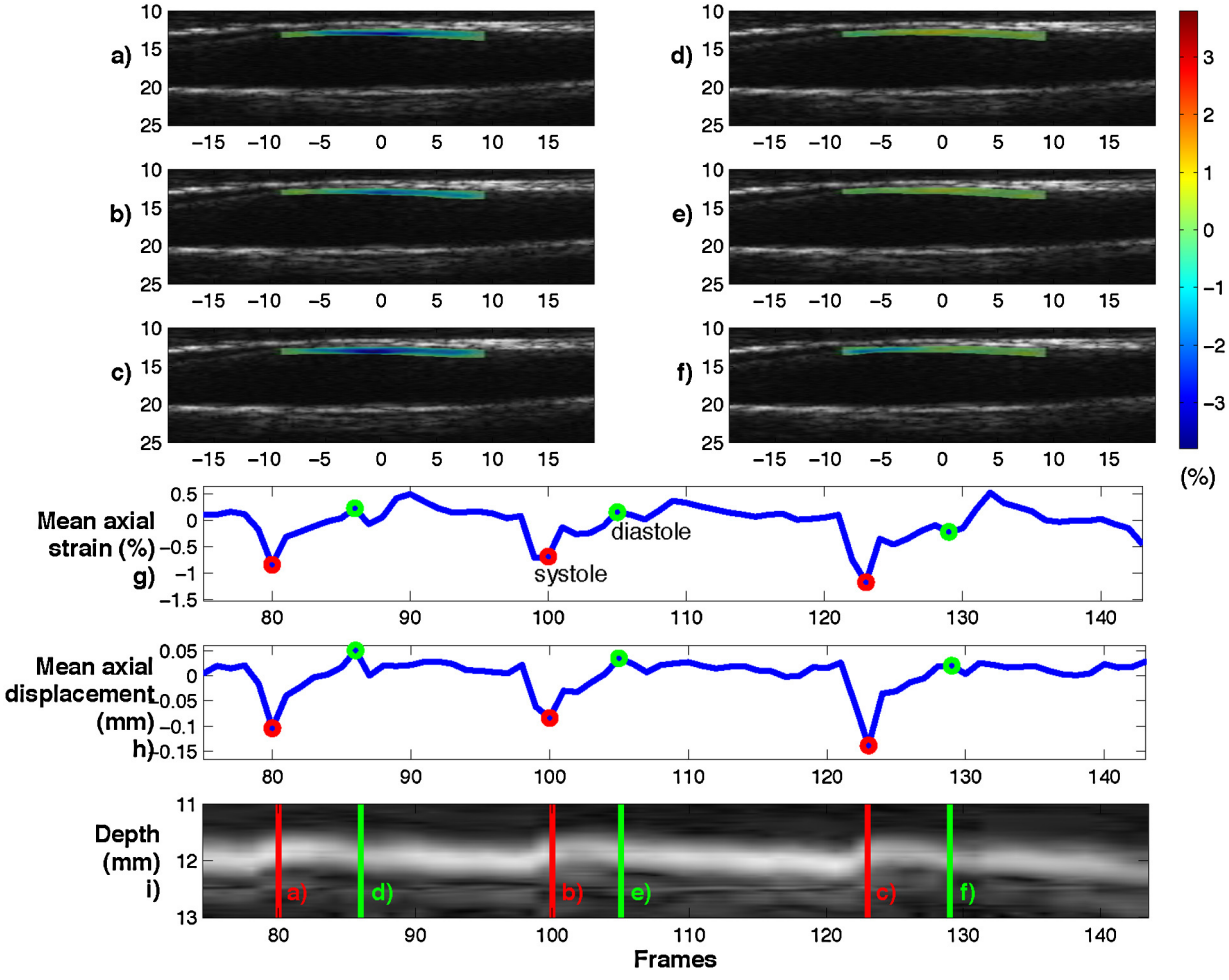

Fig. 4. Systolic axial strain elastograms (a)–(c), and diastolic elastograms (d)–(f) on three successive cardiac cycles on the near wall for a healthy subject (the dimensions of the B-mode images are in mm) corresponding to Fig. 3 (left). Mean instantaneous unfiltered axial strain and displacement over time (g) and (h) and M-mode image reconstructed from radio-frequency (RF) data (i), which were used to select the systolic and diastolic phases.

Author's personal copy

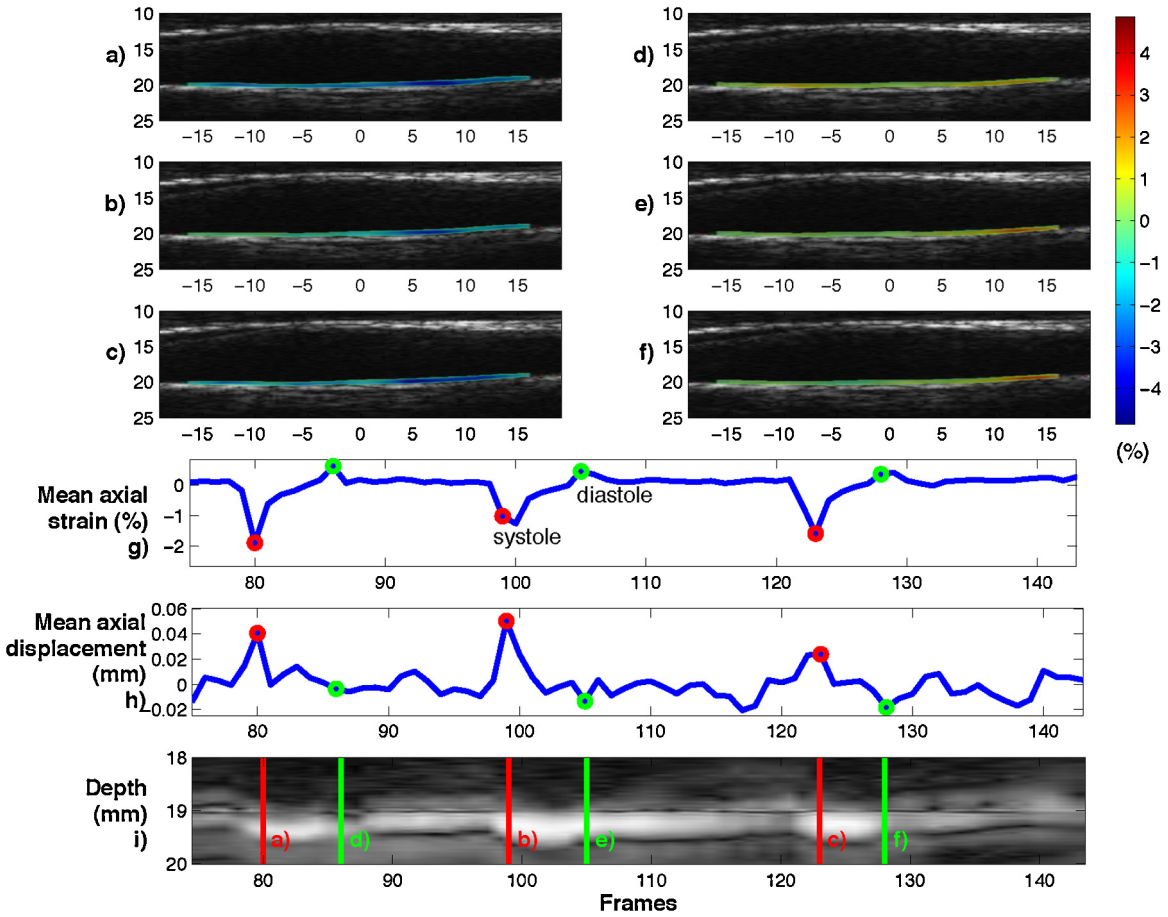

Fig. 5. Systolic axial strain elastograms (a)–(c), and diastolic elastograms (d)–(f) on three successive cardiac cycles on the far wall for a healthy subject (the dimensions of the B-mode images are in mm) corresponding to Fig. 3 (left). Mean instantaneous unfiltered axial strain and displacement over time (g) and (h) and M-mode image (i), which were used to select the systolic and diastolic phases.

3.2. Elastogram computation

The number of cardiac cycles per sequence for this study was equal to 3.9 ± 1.5. For the healthy carotids, the number of measurement windows per frame used in the computation of elastograms was equal to 306 ± 88 ($n = 3821$). For atherosclerotic arteries, this number was equal to 2253 ± 1010 ($n = 2242$). Fig. 4 shows the good reproducibility of axial strain maps for the near wall of a healthy carotid. The mean instantaneous axial strain over time is displayed with the M-mode image to indicate the good correspondence with systolic and diastolic peaks. The mean axial displacement appearing in that figure is computed as the average over the segmented wall of the y-component of the vector τ (see the paragraph before Eq. (1)). See also Fig. 5 for the far wall of the same sequence and Fig. 6 for a plaque on the far wall of an atherosclerotic carotid.

3.3. Strain curve calculation and cardiac cycle detection

Figs. 4g, 5g and 6g show the mean unfiltered instantaneous axial strain curves that were used for the localization of systolic and diastolic phases, where negative strains correspond to the vessel wall compression phase (systole) and positive strains to vessel wall stretching (diastole). The M-mode images that were used to validate that choice are displayed in Figs. 4i, 5i and 6i. As one can see from these figures, the main vessel wall tissue contraction corresponded to the instant where the wall received an impulse due to the blood flow causing its abrupt movement. Incidentally, that moment corresponds to the instant where the frame-to-frame mean axial displacement of the vessel wall was highest (hence, corresponding to a maximum velocity); see Figs. 4h, 5h and 6h.

3.4. Filtering of the instantaneous strain curves

As seen in Figs. 7 and 8 (top and middle panels), the instantaneous and cumulated strain curves show the same profile (but inverted) as a typical blood pressure curve or its gradient, respectively, throughout the cardiac cycle. As a result of filtering the original strain curves, cyclic variations were often more representative of the systolic and diastolic phases of the cardiac cycle (see Fig. 8 top). For this specific example of a case with a poor signal-to-noise ratio, the band-pass filtering allowed removing random high-frequency fluctuations; also, low-frequency time-varying breathing artifact is noted on this example, as shown in Fig. 9 top. Moreover, the filtering process allowed the computation of the strain rate over the cardiac cycle (see Fig. 8 bottom). The effect of the filtering process on the power spectrum of the axial deformation curve is illustrated for this example in Fig. 9.

3.5. Effect of the angle-dependence compensation

Using Eq. (7), the scanning angle θ was evaluated for each measurement window of all elastograms. With the corresponding angle and Eq. (6), the estimated axial strain was corrected. See Fig. 10 for

Author's personal copy

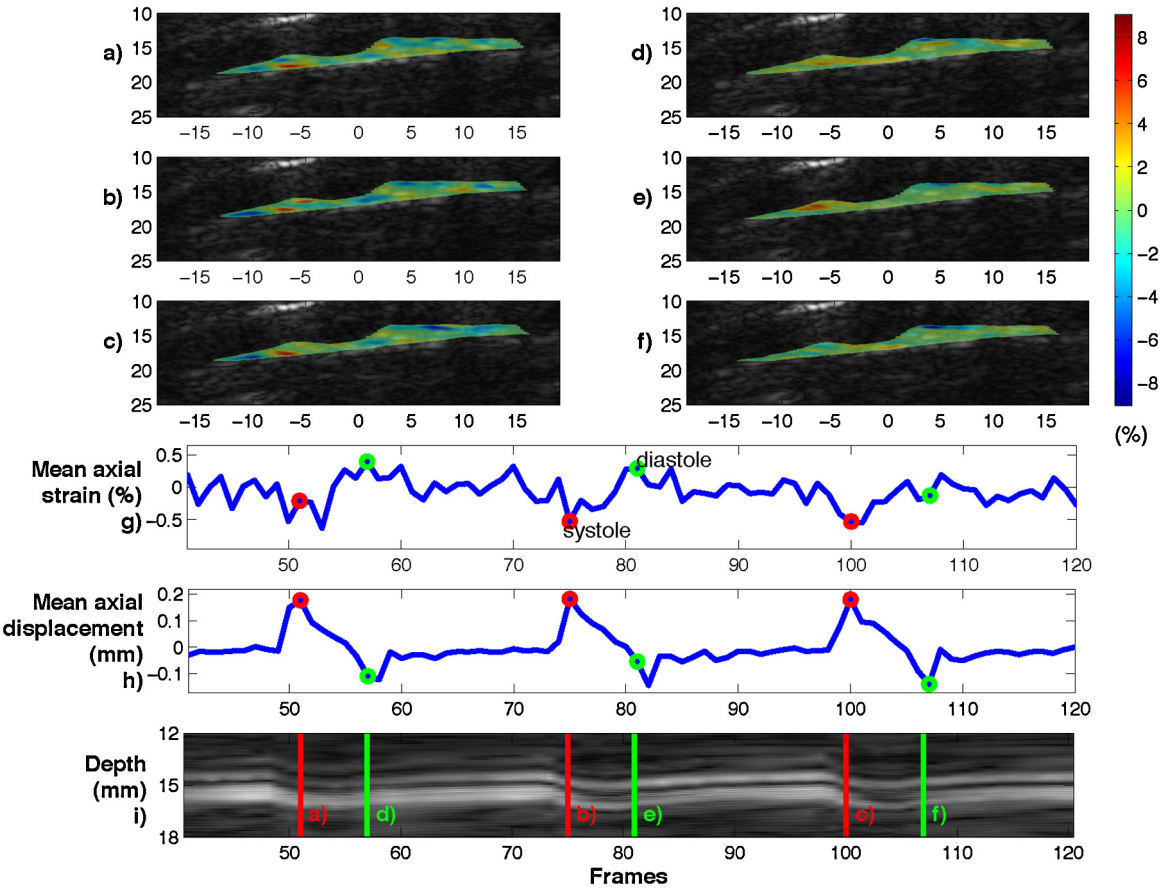

Fig. 6. Systolic axial strain elastograms (a)–(c), and diastolic elastograms (d)–(f) on three successive cardiac cycles on the far wall for a patient (the dimensions of the B-mode images are in mm) corresponding to Fig. 3 (right). Mean instantaneous unfiltered axial strain and displacement over time (g) and (h) and M-mode image (i), which were used to select the systolic and diastolic phases.

an illustration of the variation of the compensation angle over an atherosclerotic plaque on the near and far walls of a carotid artery.

The MSAS, MDAS, CAS, MaSR and MiSR values were evaluated, obtained from the filtered strain curves, before and after angle compensation. For the healthy group, the difference between non compensated and compensated parameters was statistically significant for near ($p \leq 0.01$) and far ($p \leq 4 \times 10^{-5}$) walls. For the atherosclerotic group, this difference was also significant for the near wall ($p \leq 5 \times 10^{-4}$) and for the far wall, it was significantly different ($p \leq 0.02$), except for the MiSR value that was close to significance ($p = 0.06$). See Table 1 for more details.

3.6. Strain difference between near and far walls and between populations

The MSAS, MDAS and CAS values were calculated after angle compensation and filtering of the strain curve as well as MaSR and MiSR. For healthy subjects, paired *t*-tests showed statistically

Table 1
Mean (in % or $\%\,s^{-1}$) and coefficient of variation (CV = standard deviation/absolute value of mean) of five strain parameters (after filtering) for far and near walls of healthy and atherosclerotic subjects without or with angle compensation (AC).

Group	Wall	AC	MSAS[a]		MDAS[b]		CAS[c]		MiSR[d]		MaSR[e]	
			Mean	CV	Mean	CV	Mean	CV	Mean	CV	Mean	CV
Healthy ($n = 30$)	Far	No	−0.31	0.70	0.35	0.64	1.79	0.53	−3.34	0.51	4.17	0.52
		Yes	−0.33*	0.68	0.38*	0.62	1.94*	0.52	−3.68*	0.49	4.49*	0.50
Healthy ($n = 30$)	Near	No	−0.19	0.81	0.24	0.89	1.16	0.71	−2.17	0.94	2.30	0.68
		Yes	−0.22*	0.84	0.27*	0.80	1.33*	0.72	−2.46*	0.87	2.64*	0.71
Patho ($n = 21$)	Far	No	−0.20	0.75	0.24	1.06	1.49	0.85	−1.66	0.84	2.02	0.82
		Yes	−0.23*	0.83	0.28*	1.05	1.71*	0.85	−1.89 (p=0.06)	0.97	2.29*	0.88
Patho ($n = 21$)	Near	No	−0.18	0.86	0.22	0.75	1.26	0.63	−1.74	1.06	1.98	1.05
		Yes	−0.20*	0.83	0.25*	0.68	1.41*	0.58	−1.96*	0.99	2.21*	0.98

[a] Mean systolic axial strain.
[b] Mean diastolic axial strain.
[c] Cumulated axial strain.
[d] Minimum strain rate.
[e] Maximum strain rate.
* Represents a statistically significant difference between AC or no AC obtained from paired *t*-tests.

Author's personal copy

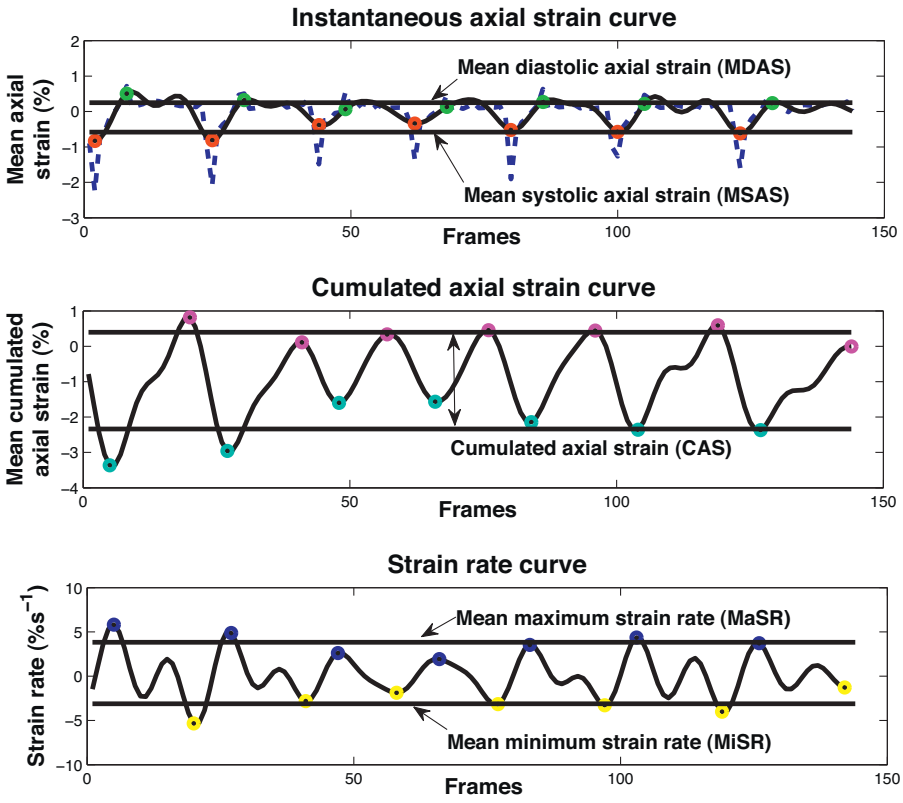

Fig. 7. Top: Original (dashed blue) and filtered (black) instantaneous strain curves of the far wall of the left internal carotid of a healthy subject over seven consecutive cardiac cycles, with systolic (red) and diastolic (green) points indicated. Middle: corresponding cumulated strain curve (black) calculated from the filtered instantaneous strain curve, with minima (cyan) and maxima (magenta) indicated on each cycle. Bottom: strain rate curve (black) obtained from the filtered instantaneous strain curve, with minima (yellow) and maxima (blue) indicated on each cycle. See Fig. 5 for the corresponding elastograms, mean displacement curve and M-mode. (For interpretation of the references to color in this figure legend, the reader is referred to the web version of the article.)

significant differences ($p \leq 0.02$) between near and far walls for all strain parameters (see Table 2). For the atherosclerotic group, no statistically significant differences ($p \leq 0.44$) between near and far plaques were observed (Table 2).

Statistically significant differences were found between healthy and atherosclerotic carotid arteries, for MaSR ($p = 0.001$) and MiSR ($p = 8 \times 10^{-4}$) parameters of the far wall (see Table 3, which presents results of Table 2 by emphasizing differences between groups). The receiver operating characteristic (ROC) curve was computed for these two parameters (by varying the threshold that classifies healthy from atherosclerotic carotid arteries). The area under the ROC curve (AUC) was equal to 0.842 for the MaSR parameter and equal to 0.828 for the MiSR parameter. We also found that there were significant differences between healthy and atherosclerotic carotid arteries, for MaSR ($p = 5 \times 10^{-4}$) and MiSR ($p = 4 \times 10^{-4}$) parameters of the far wall, when no angle compensation was applied. The AUC for the corresponding ROC curves were equal to 0.837 and 0.826 for the MaSR and MiSR parameters, respectively. See Fig. 11 for an illustration of the ROC curves.

There were statistically significant differences between healthy and atherosclerotic carotid arteries, for MSAS ($p = 0.019$), MDSA ($p = 0.002$) and CAS ($p = 0.017$) parameters of the far wall after angle compensation and normalization by the pressure gradient (see Table 4). The area under the ROC curve (AUC) was equal to 0.696 for the MSAS parameter, 0.762 for the MDAS and equal to 0.699 for the CAS parameter.

Table 2
Mean (in % or % s^{-1}) and coefficient of variation (CV = standard deviation/absolute value of mean) of five strain parameters (after filtering and angle compensation) for far and near walls of healthy and atherosclerotic subjects.

Group	Wall	MSAS[a]		MDAS[b]		CAS[c]		MiSR[d]		MaSR[e]	
		Mean	CV	Mean	CV	Mean	CV	Mean	CV	Mean	CV
Healthy ($n = 30$)	Far	−0.33	0.68	0.38	0.62	1.94	0.52	−3.68	0.49	4.49	0.50
	Near	−0.22*	0.84	0.27*	0.80	1.33*	0.72	−2.46*	0.87	2.64*	0.71
Patho ($n = 21$)	Far	−0.23	0.83	0.28	1.05	1.71	0.85	−1.89	0.97	2.29	0.88
	Near	−0.20	0.83	0.25	0.68	1.41	0.58	−1.96	0.99	2.21	0.98

[a] Mean systolic axial strain.
[b] Mean diastolic axial strain.
[c] Cumulated axial strain.
[d] Minimum strain rate.
[e] Maximum strain rate.
* Represents a statistically significant difference between far and near walls obtained from paired *t*-tests.

Author's personal copy

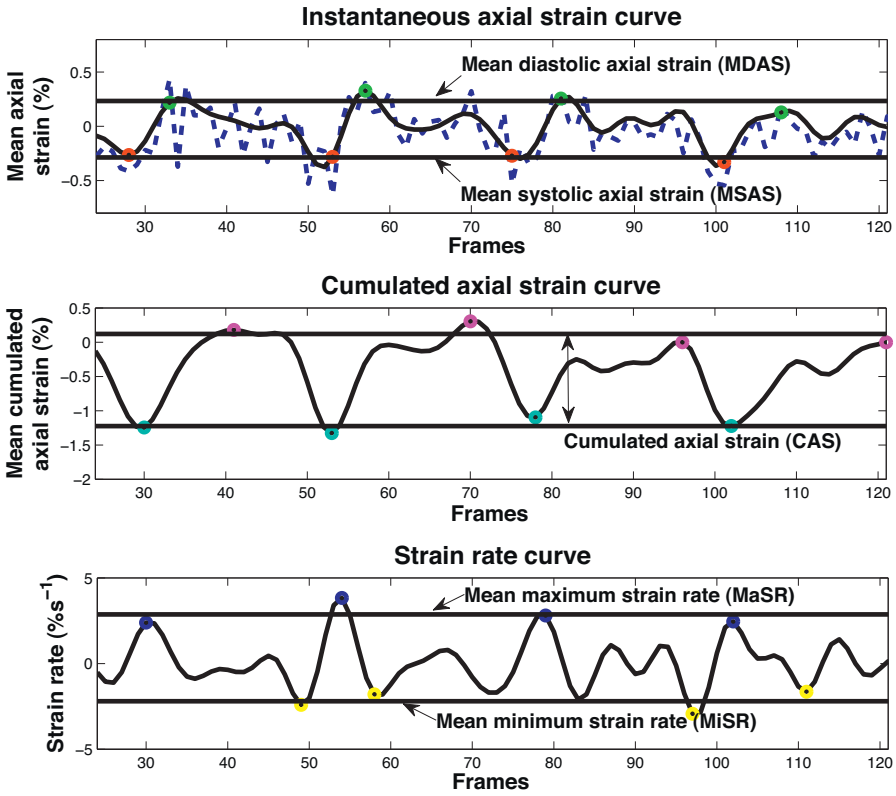

Fig. 8. Top: Original (dashed blue) and filtered (black) instantaneous strain curves of a plaque located on the far wall of the left internal carotid of a patient over four consecutive cardiac cycles, with systolic (red) and diastolic (green) points indicated. Middle: corresponding cumulated strain curve (black) calculated from the filtered instantaneous strain curve, with minima (cyan) and maxima (magenta) indicated on each cycle. Bottom: strain rate curve (black) obtained from the filtered instantaneous strain curve, with minima (yellow) and maxima (blue) indicated on each cycle. See Fig. 6 for the corresponding elastograms, mean displacement curve and M-mode. (For interpretation of the references to color in this figure legend, the reader is referred to the web version of the article.)

Table 3
Mean (in % or % s^{-1}) and coefficient of variation (CV = standard deviation/absolute value of mean) of five strain parameters for near and far walls of healthy and atherosclerotic subjects. Note that values are the same as Table 2, but they are reorganized to emphasize differences between groups.

Wall	Group	MSAS[a]		MDAS[b]		CAS[c]		MiSR[d]		MaSR[e]	
		Mean	CV	Mean	CV	Mean	CV	Mean	CV	Mean	CV
Far	Healthy (n = 30)	−0.33	0.68	0.38	0.62	1.94	0.52	−3.68	0.49	4.49	0.50
	Patho (n = 21)	−0.23	0.83	0.28	1.05	1.71	0.85	−1.89*	0.97	2.29*	0.88
Near	Healthy (n = 30)	−0.22	0.84	0.27	0.80	1.33	0.72	−2.46	0.87	2.64	0.71
	Patho (n = 21)	−0.20	0.83	0.25	0.68	1.41	0.58	−1.96	0.99	2.21	0.98

[a] Mean systolic axial strain.
[b] Mean diastolic axial strain.
[c] Cumulated axial strain.
[d] Minimum strain rate.
[e] Maximum strain rate.
* Represents a statistically significant difference between healthy and atherosclerotic subjects obtained from t-tests.

Table 4
Mean (in % mm Hg^{-1}) and coefficient of variation (CV = standard deviation/absolute value of mean) of three strain parameters for near and far walls of healthy and atherosclerotic subjects corrected for the pressure gradient between two consecutive RF images.

Wall	Group	MSAS[a]		MDAS[b]		CAS[c]	
		Mean	CV	Mean	CV	Mean	CV
Far	Healthy (n = 30)	−0.103	0.71	0.124	0.64	0.627	0.51
	Patho (n = 21)	−0.060*	0.92	0.068*	0.99	0.443*	0.85
Near	Healthy (n = 30)	−0.072	0.88	0.095	1.02	0.455	0.82
	Patho (n = 21)	−0.046	0.64	0.059	0.70	0.343	0.59

[a] Mean systolic axial strain.
[b] Mean diastolic axial strain.
[c] Cumulated axial strain.
* Represents a statistically significant difference between healthy and atherosclerotic subjects obtained from t-tests.

Author's personal copy

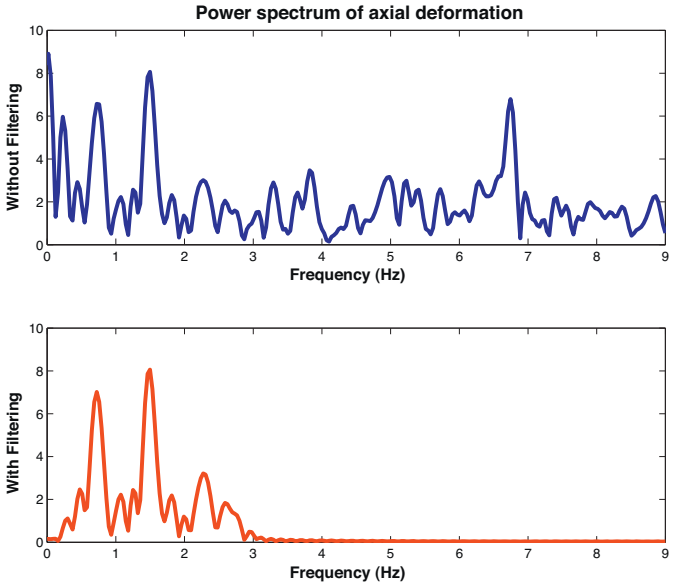

Fig. 9. Example of the power spectrum of the axial deformation curve before (top) and after (bottom) applying the filtering process, corresponding to the instantaneous strain curves of Fig. 8.

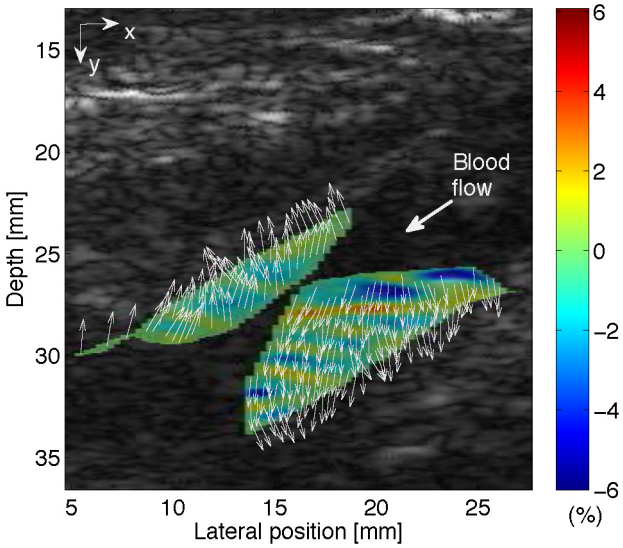

Fig. 10. Illustration of the variation of the compensation angle θ over an atherosclerotic plaque on the near and far walls of a carotid artery. On the far wall, the arrows represent the unit vectors y_0 computed on each region-of-interest (ROI) and forming a local angle θ with the y-axis; for the near wall, the angles $180-\theta$ are displayed. See Fig. 2 for a schematic representation of the local angle θ. The color scale represents the axial strain (after angle compensation) indicating compression with spatial average values of −0.5% in the near wall and of −0.67% in the far wall. Note that the density of vectors was reduced to facilitate the visual interpretation. Also notice that the direction of deformations are not only determined by the blood pressure pulsation, but also by the blood flow direction. (For interpretation of the references to color in this figure legend, the reader is referred to the web version of the article.)

4. Discussion

Conventional elastographic algorithms use cross-correlation techniques in small ROIs, combined with a multiscale approach [71], temporal stretching [72], and/or interpolation [47] to estimate the displacement. Then, from the displacement field, strain components are derived using a least-squares strain estimator [73]. Those temporal approaches make the assumption that in each ROI, the displacement field is constant. Unlike these methods, the LSME does not assume that the displacement field in the given ROI is constant, but rather that it follows a linear model, which is theoretically stronger. Furthermore, as the LSME method computes the full 2D displacement gradient matrix from the RF data, it does not depend on possible outliers present in a pre-computed displacement field. Moreover, unlike usual strain estimators, the LSME method does not require a direct computation of displacement gradients to compute the 2D displacement gradient matrix. We thus believe that the LSME is more reliable than cross-correlation techniques.

Concerning the elastogram computation (Section 2.4), important overlapping between measurement windows is not unusual; see for instance [19,44,45,52,71]. Such overlapping between measurement windows results in correlations between the corresponding measures on adjacent pixels. This fact implies a spatial consistency of the measures within the image; see Figs. 4–6 and 10.

Concerning the angle-dependance compensation method (Section 2.6), note that both hypotheses (H2) and (H3) do not imply the absence of motion along the x_0-axis; indeed, a non-vanishing constant translation component along that axis is allowed in the proposed model. One of the limitations of the proposed model is that motion out of the image plane is not measurable. Fortunately, under the proposed hypotheses, the expression of the compensation angle amplitude does not depend on the measurement of the lateral strain component $\varepsilon^{\theta}_{xx} = \Delta^{\theta}_{xx}$, which is not reliable [49].

The instantaneous strain values obtained in the present study are consistent with the values reported in the previous study on

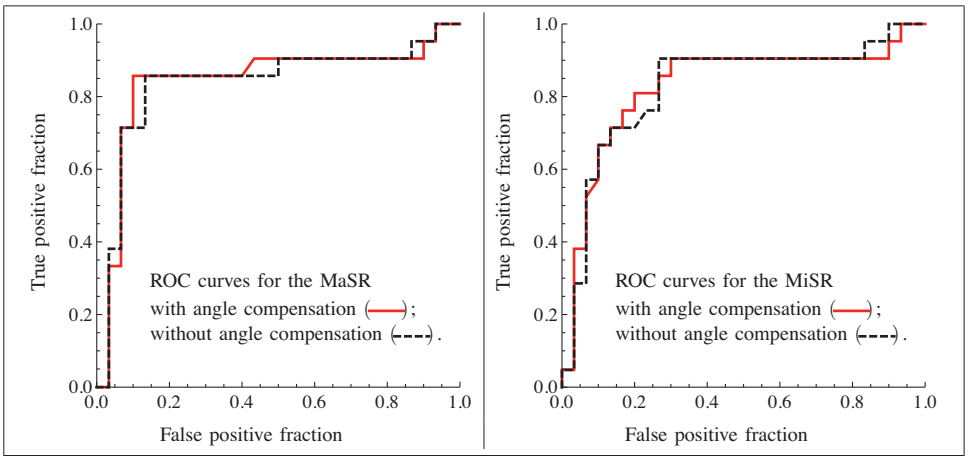

Fig. 11. Receiver operating characteristic (ROC) curves for the maximum strain rate (MaSR) and minimum strain rate (MiSR) parameters with and without angle compensation.

Author's personal copy

NIVE [45], which in turn were shown to be consistent with the distensibility values reported in [74–76]; see also the values reported in [41] (but the age range of the patients is not indicated in that reference).

We evaluated the difference in the strain behavior between near and far walls of the carotid artery because we hypothesized that both walls could be subjected to different stress conditions. Indeed, the near wall motion can be restricted by the pressure applied by the ultrasound probe during examination and RF data acquisition [77]. In the same way, movements of the far wall can be limited by other anatomical structures, such as a cervical vertebra. Also, the fascia that surrounds the carotid artery can affect movements of both walls in a different way. Thus, the difference in the strain behavior between near and far walls of the carotid artery could be explained by the fact that both walls are not subjected to the same stress conditions. A recent article also showed a difference between near and far walls of a healthy common carotid artery in term of mean displacements [78]. They imputed this to the location of the wall relative to the region of the acoustic radiation force impulse (ARFI) of the ARFI imaging method. But for both ARFI and NIVE methods, the pressure applied by the ultrasound probe can also be seen as a mechanical excitation source. Further investigations are required to confirm these assumptions and explain differences in behavior between normal and atherosclerotic carotid walls, by considering limiting boundary conditions. In fact, the far wall of the artery is surrounded by more rigid structures (paraspinal muscles and cervical spine) than the near wall, mainly surrounded by the sternocleidomastoid muscle and jugular vein in an antero lateral position. This allows the near wall to have greater displacements than the far wall due to less limiting constraints and thus lower strain. Furthermore, it is known that atherosclerotic arteries are more rigid than healthy ones. In that case, we believe that differences in limiting conditions between the near and far walls have less impact on the strain behavior of the arterial wall than the displacement behavior. Meanwhile, we suggest to analyze the near and far walls in an independent manner.

Longitudinal scans of the carotid artery in non-invasive elastography can be difficult to achieve, especially for the proximal internal carotid section. This section of the artery is often tortuous, deeper than the common artery and located behind the external carotid. The bifurcation site can also be hard to reach, but these two locations (proximal internal carotid and carotid bifurcation) are prone to atherosclerosis development because of hemodynamic perturbations. By comparing the present study to [45], we noticed less artifacts on time-varying strain curves of healthy common carotids than healthy and atherosclerotic internals. This may not only be attributed to the state of the artery but to its location and tortuosity.

An angle between the plane perpendicular to the principal axis of the vessel and the ultrasound beam direction causes an underestimation of the estimated axial strain. This angle dependence was evaluated in IVUS [50] and the same relation as in Eq. (6) was obtained for the radial component of the strain, but the angle was estimated from the position of the catheter in the lumen. In the proposed method, the goal was to find the direction in the image plane corresponding to the plane strain condition. Since the strain orientation within each measurement window is likely to be different for a heterogeneous plaque, a local compensative model was proposed. The difference between non compensated and compensated estimates was statistically significant for almost all strain parameters of the two groups (Table 1). However, when considering the discriminant power of the MaSR and MiSR parameters on the far wall to distinguish between healthy and atherosclerotic arteries, it was found that the AUC of the corresponding ROC curves were identical with or without angle compensation. From Fig. 10, the local compensation angle seems to depend on the intraluminal pressure and the blood flow, and not only on the global angle between the artery and the ultrasound beam direction. In the field of echocardiography, velocity vector imaging (VVI) has been proposed to assess quantitatively myocardial acceleration in normal left ventricle [79], myocardial dysfunction [80], or left ventricular dyssynchrony [81]. As mentioned in [79, Discussion, p. 814], the velocity vector field is equivalent to the local frame-to-frame displacement. In Fig. 10, a different vector field was proposed: the field of unit vectors in the direction of the plane strain condition. In particular, the translation term in the displacement field is removed from the proposed vector field, and there remains only information about the local deformation.

Also, a filtering process was introduced to remove motion artifacts (see Section 2.7). It resulted in a smoother strain curve from which strain rate values were extracted. These parameters (MaSR and MiSR – see Table 3) allowed to differentiate healthy and atherosclerotic carotid arteries. The visual distinction on an elastogram between an atherosclerotic lesion and its surrounding normal tissues has already been demonstrated [44], but so far, no elastographic study gave evidence of significant quantitative differences between normal and diseased subjects paired for age. However, axial strains of healthy walls and plaques from 12 patients were compared in [41] in the context of NIVE.

The variable frame rate, heart rate and pressure pulse can be confounding variables in the computation of the strain parameters. However, these variables can be combined to yield an estimation of the pressure gradient (as in [45]), which represents the pressure step between two successive frames. Thus, normalizing the strain parameters with the pressure gradient is an empirical method for reducing the effect of the differences in frame rate, heart rate and pressure pulse among the various acquisitions of RF data sequences. From this point of view, it is important to record these variables at the time of acquisition. Note that the MSAS, MDAS and CAS present statistically significant differences between healthy and atherosclerotic carotids only after compensation by the pressure gradient.

In this study, original and promising clinical indexes based on maximal and minimal axial strain rate amplitudes were successfully used to highlight atherosclerotic subjects. However, knowing that plaques are heterogeneous (namely, they are constituted of calcium, lipids and fibrosis), it would be desirable to implement a segmentation process that would be able to distinguish the main plaque components and thus allow a better diagnosis regarding the risk of rupture. Indeed, it could be easier to interpret the mean axial curves (such as in Fig. 6g) obtained by averaging the strain elastograms on each component of the plaque, since one would avoid blending different types of elastograms together (corresponding to different tissue components).

As seen in Figs. 4a–f and 5a–f, the variations in axial strain along the wall might be quite large. Since these instantaneous strain maps are taken at specific moments in the cardiac cycle, one might expect more homogeneity in their values. However, it is known that blood pressure induces a wave that propagates along the artery (the propagation of the pressure wave was measured in [82,83]), and hence, is not a homogeneous constraint applied to the vessel wall. We think that such a spatial variation in the pressure field explains the local variation in the strain maps presented in Figs. 4a–f and 5a–f. We believe that this phenomenon is not necessarily a drawback for the assessment of early signs of atherosclerosis (arterial stiffness) or plaque characterization. Indeed, as of now, the Young modulus mapping of vulnerable plaques has been successfully implemented [16,36] based on the elastograms computed with the LSME model, in the context of plaque characterization of coronary arteries with intravascular ultrasound imaging. Recently, a relative elastic modulus reconstruction method was proposed [84] in the context of NIVE. As mentioned above, a segmentation tool to distinguish the

Author's personal copy

various plaque components and evaluate their mechanical properties could be useful.

Hopefully, the strain rate parameters or the normalized strain parameters combined with a local analysis of the strain maps may make possible the prospective differentiation of stable versus vulnerable unstable plaques. Although this task has not been proven yet with NIVE, it has been shown [46] that NIVE is feasible in patients with significant carotid stenosis and can detect the presence of a lipid core with high sensitivity and moderate specificity.

5. Conclusions

Determining the vulnerability of human atherosclerotic plaques to rupture in order to prevent stroke would be greatly beneficial to patients' health. Since the rupture of a plaque is related to its mechanical properties, the resulting axial strain maps have been studied in this paper. The robustness of these measurements to the great variability of acquisition conditions in a clinical context is a desirable property. In this paper, an angle-compensation method was proposed to take into account locally on each measurement window the plane strain condition to avoid underestimation of the estimated axial strain. The proposed angle-compensation method used the (non-compensated) axial strain and axial and lateral shears to produce the compensated axial strain. The difference between non compensated and compensated estimates was statistically significant for almost all strain parameters of the two groups. The mean systolic, mean diastolic and cumulated axial strains after normalization by the pressure gradient, as well as the proposed maximum and minimum strain rates, which are computed from the axial strain curves, allowed to differentiate healthy and atherosclerotic carotid arteries. The area under the ROC curves for these two strain rate parameters were almost identical with or without angle compensation and was larger than the area under the ROC curves for the three normalized strain parameters. Despite this fact, we believe that the compensation angle variation map over an atherosclerotic plaque might be an indicator of plaque vulnerability. It may indeed reveal zones with heterogeneous mechanical structures deforming according to different angulations. This hypothesis should be studied in future work.

Acknowledgments

This research was supported by a joint international program of the ANR (MELANII project # 09-BLANC-0423, Dr. J. Ohayon) and Natural Sciences and Engineering Research Council of Canada strategic grant (# STPGP-381136-09, Dr. G. Cloutier).

References

[1] Thom T, Haase N, Rosamond W, Howard VJ, Rumsfeld J, Manolio T, et al. Heart disease and stroke statistics – 2006 update. Circulation 2006;113(6):e85–151.
[2] Casscells W, Naghavi M, Willerson JT. Vulnerable atherosclerotic plaque. Circulation 2003;107(16):2072–5.
[3] Nandalur KR, Baskurt E, Hagspiel KD, Phillips CD, Kramer CM. Calcified carotid atherosclerotic plaque is associated less with ischemic symptoms than is non-calcified plaque on MDCT. Am J Roentgenol 2005;184(1):295–8.
[4] Naghavi M, Falk E. From vulnerable plaque to vulnerable patients. In: Naghavi M, editor. Asymptomatic atherosclerosis: pathophysiology, detection and treatment. Humana Press; 2010. p. 13–38.
[5] Cheng GC, Loree HM, Kamm RD, Fishbein MC, Lee RT. Distribution of circumferential stress in ruptured and stable atherosclerotic lesions. A structural analysis with histopathological correlation. Circulation 1993;87(4):1179–87.
[6] Loree HM, Kamm RD, Stringfellow RG, Lee RT. Effects of fibrous cap thickness on peak circumferential stress in model atherosclerotic vessels. Circ Res 1992;71(4):850–8.
[7] Finet G, Ohayon J, Rioufol G. Biomechanical interaction between cap thickness, lipid core composition and blood pressure in vulnerable coronary plaque: impact on stability or instability. Coron Artery Dis 2004;15(1):13–20.
[8] Finet G, Ohayon J, Rioufol G, Lefloch S, Tracqui P, Dubreuil O, et al. Morphological and biomechanical aspects of vulnerable coronary plaque. Arch Mal Coeur Vaiss 2007;100(6–7):547–53.
[9] Alfonso F, Macaya C, Goicolea J, Hernandez R, Segovia J, Zamorano J, et al. Determinants of coronary compliance in patients with coronary artery disease: an intravascular ultrasound study. J Am Coll Cardiol 1994;23(4):879–84.
[10] Beaussier H, Naggara O, Calvet D, Joannides R, Guegan-Massardier E, Gerardin E, et al. Mechanical and structural characteristics of carotid plaques by combined analysis with echotracking system and MR imaging. JACC Cardiovasc Imag 2011;4(5):468–77.
[11] Godia EC, Madhok R, Pittman J, Trocio S, Ramas R, Cabral D, et al. Carotid artery distensibility. J Ultrasound Med 2007;26(9):1157–65.
[12] O'Rourke MF, Staessen JA, Vlachopoulos C, Duprez D, Plante GE. Clinical applications of arterial stiffness; definitions and reference values. Am J Hypertens 2002;15(5):426–44.
[13] Baldewsing RA, Mastik F, Schaar JA, Serruys PW, van der Steen AFW. Young's modulus reconstruction of vulnerable atherosclerotic plaque components using deformable curves. Ultrasound Med Biol 2006;32(2):201–10.
[14] Doyley MM, Mastik F, de Korte CL, Carlier SG, Cespedes EI, Serruys PW, et al. Advancing intravascular ultrasonic palpation toward clinical applications. Ultrasound Med Biol 2001;27(11):1471–80.
[15] Le Floc'h S, Cloutier G, Saijo Y, Finet G, Yazdani SK, Deleaval F, et al. A four-criterion selection procedure for atherosclerotic plaque elasticity reconstruction based on in vivo coronary intravascular ultrasound radial strain sequences. Ultrasound Med Biol 2013;38(12):2084–97.
[16] Le Floc'h S, Ohayon J, Tracqui P, Finet G, Gharib AM, Maurice RL, et al. Vulnerable atherosclerotic plaque elasticity reconstruction based on a segmentation-driven optimization procedure using strain measurements: theoretical framework. IEEE Trans Med Imag 2009;28(7):1126–37.
[17] Parker KJ, Doyley MM, Rubens DJ. Imaging the elastic properties of tissue: the 20 year perspective. Phys Med Biol 2011;56(1):R1–29.
[18] Ophir J, Cespedes I, Ponnekanti H, Yazdi Y, Li X. Elastography: a quantitative method for imaging the elasticity of biological tissues. Ultrason Imaging 1991;13(2):111–34.
[19] de Korte CL, van der Steen AF, Céspedes EI, Pasterkamp G, Carlier SG, Mastik F, et al. Characterization of plaque components and vulnerability with intravascular ultrasound elastography. Phys Med Biol 2000;45(6):1465–75.
[20] de Korte CL, van Der Steen AFW. Intravascular ultrasound elastography: an overview. Ultrasonics 2002;40(1):859–65.
[21] de Korte CL, Sierevogel MJ, Mastik F, Strijder C, Schaar JA, Velema E, et al. Identification of atherosclerotic plaque components with intravascular ultrasound elastography in vivo: a Yucatan pig study. Circulation 2002;105(14):1627–30.
[22] Schaar JA, de Korte CL, Mastik F, Strijder C, Pasterkamp G, Boersma E, et al. Characterizing vulnerable plaque features with intravascular elastography. Circulation 2003;108(21):2636–41.
[23] Perrey C, Braeker G, Bojara W, Lindstaedt M, Holt S, Ermert H. Strain imaging with intravascular ultrasound array scanners: validation with phantom experiments. Biomed Tech/Biomed Eng 2003;48(5):135–40.
[24] Maurice RL, Ohayon J, Finet G, Cloutier G. Adapting the Lagrangian speckle model estimator for endovascular elastography: theory and validation with simulated radio-frequency data. J Acoust Soc Am 2004;116(2):1276–86.
[25] Maurice RL, Brusseau É, Finet G, Cloutier G. On the potential of the Lagrangian speckle model estimator to characterize atherosclerotic plaques in endovascular elastography: in vitro experiments using an excised human carotid artery. Ultrasound Med Biol 2005;31(1):85–91.
[26] Maurice RL, Fromageau J, Brusseau É, Finet G, Rioufol G, Cloutier G. On the potential of the Lagrangian estimator for endovascular ultrasound elastography: in vivo human coronary artery study. Ultrasound Med Biol 2007;33(8):1199–205.
[27] Maurice RL, Fromageau J, Roy Cardinal M-H, Doyley M, Demuinck E, Robb J, et al. Characterization of atherosclerotic plaques and mural thrombi with intravascular ultrasound elastography: a potential method evaluated in an aortic rabbit model and a human coronary artery. IEEE Trans Inform Technol Biomed 2008;12(3):290–8.
[28] Katouzian A, Sathyanarayana S, Baseri B, Konofagou EE, Carlier S. Challenges in atherosclerotic plaque characterization with intravascular ultrasound (IVUS): from data collection to classification. IEEE Trans Inform Technol Biomed 2008;12(3):315–27.
[29] Liang Y, Zhu H, Gehrig T, Friedman MH. Measurement of the transverse strain tensor in the coronary arterial wall from clinical intravascular ultrasound images. J Biomech 2008;41(14):2906–11.
[30] Liang Y, Zhu H, Friedman MH. Estimation of the transverse strain tensor in the arterial wall using IVUS image registration. Ultrasound Med Biol 2008;34(11):1832–45.
[31] Liang Y, Zhu H, Friedman MH. Measurement of the 3D arterial wall strain tensor using intravascular B-mode ultrasound images: a feasibility study. Phys Med Biol 2010;55(21):6377–94.
[32] Hu X-B, Zhang P-F, Su H-J, Yi X, Chen L, Rong Y-Y, et al. Intravascular ultrasound area strain imaging used to characterize tissue components and assess vulnerability of atherosclerotic plaques in a rabbit model. Ultrasound Med Biol 2011;37(10):1579–87.
[33] Doyley MM, Meaney PM, Bamber JC. Evaluation of an iterative reconstruction method for quantitative elastography. Phys Med Biol 2000;45(6):1521–40.
[34] Doyley MM, Srinivasan S, Pendergrass SA, Wu Z, Ophir J. Comparative evaluation of strain-based and model-based modulus elastography. Ultrasound Med Biol 2005;31(6):787–802.
[35] Baldewsing RA, Schaar JA, Mastik F, Oomens CW, van der Steen AF. Assessment of vulnerable plaque composition by matching the deformation of a

Author's personal copy

parametric plaque model to measured plaque deformation. IEEE Trans Med Imag 2005;24(4):514–28.
[36] Le Floc'h S, Cloutier G, Finet G, Tracqui P, Pettigrew R, Ohayon J. On the potential of a new IVUS elasticity modulus imaging approach for detecting vulnerable atherosclerotic coronary plaques: in vitro vessel phantom study. Phys Med Biol 2010;55(19):5701–21.
[37] Richards MS, Doyley MM. Investigating the impact of spatial priors on the performance of model-based IVUS elastography. Phys Med Biol 2011;56(22):7223–46.
[38] Richards MS, Doyley MM. Non-rigid image registration based strain estimator for intravascular ultrasound elastography. Ultrasound Med Biol 2012;39(3):515–33.
[39] Golemati S, Sassano A, Lever MJ, Bharath AA, Dhanjil S, Nicolaides AN. Carotid artery wall motion estimated from B-mode ultrasound using region tracking and block matching. Ultrasound Med Biol 2003;29(3):387–99.
[40] Kanai H, Hasegawa H, Ichiki M, Tezuka F, Koiwa Y. Elasticity imaging of atheroma with transcutaneous ultrasound: preliminary study. Circulation 2003;107(24):3018–21.
[41] Ribbers H, Lopata RG, Holewijn S, Pasterkamp G, Blankensteijn JD, de Korte CL. Noninvasive two-dimensional strain imaging of arteries: validation in phantoms and preliminary experience in carotid arteries in vivo. Ultrasound Med Biol 2007;33(4):530–40.
[42] Shi H, Mitchell CC, McCormick M, Kliewer MA, Dempsey RJ, Varghese T. Preliminary in vivo atherosclerotic carotid plaque characterization using the accumulated axial strain and relative lateral shift strain indices. Phys Med Biol 2008;53(22):6377–94.
[43] Maurice RL, Ohayon J, Frétigny Y, Bertrand M, Soulez G, Cloutier G. Non-invasive vascular elastography: theoretical framework. IEEE Trans Med Imag 2004;23(2):164–80.
[44] Schmitt C, Soulez G, Maurice RL, Giroux M-F, Cloutier G. Non-invasive vascular elastography: toward a complementary characterization tool of atherosclerosis in carotid arteries. Ultrasound Med Biol 2007;33(12):1841–58.
[45] Maurice RL, Soulez G, Giroux MF, Cloutier G. Noninvasive vascular elastography for carotid artery characterization on subjects without previous history of atherosclerosis. Med Phys 2008;35(8):3436–43.
[46] Naim C, Cloutier G, Mercure E, Destrempes F, Qin Z, El-Abyad W, et al. Characterisation of carotid plaques with ultrasound elastography: feasibility and correlation with high-resolution magnetic resonance imaging. Eur Radiol 2013;23(7):2030–41.
[47] Konofagou E, Ophir J. A new elastographic method for estimation and imaging of lateral displacements, lateral strains, corrected axial strains and Poisson's ratios in tissues. Ultrasound Med Biol 1998;24(8):1183–99.
[48] Varghese T, Ophir J, Konofagou E, Kallel F, Righetti R. Tradeoffs in elastographic imaging. Ultrason Imaging 2001;23(4):216–48.
[49] Mercure E, Cloutier G, Schmitt C, Maurice R. Performance evaluation of different implementations of the Lagrangian speckle model estimator for non-invasive vascular ultrasound elastography. Med Phys 2008;35(7):3116–26.
[50] de Korte CL, Cespedes EI, van Der Steen AW. Influence of catheter position on estimated strain in intravascular elastography. IEEE Trans Ultrason Ferroelectr Freq Control 1999;46(3):616–25.
[51] Shi H, Chen Q, Varghese T. A general solution for catheter position effects for strain estimation in intravascular elastography. Ultrasound Med Biol 2005;31(11):1509–26.
[52] Mercure E, Deprez J-F, Fromageau J, Basset O, Soulez G, Cloutier G, et al. A compensative model for the angle-dependence of motion estimates in noninvasive vascular elastography. Med Phys 2011;38(2):727–35.
[53] Rao M, Varghese T. Spatial angular compounding for elastography without the incompressibility assumption. Ultrason Imaging 2005;27(4):256–70.
[54] Rao M, Varghese T. Correlation analysis of the beam angle dependence for elastography. J Acoust Soc Am 2006;119(6):4093–101.
[55] Rao M, Chen Q, Shi H, Varghese T, Madsen EL, Zagzebski JA, et al. Normal and shear strain estimation using beam steering on linear-array transducers. Ultrasound Med Biol 2007;33(1):57–66.
[56] Hansen HHG, Lopata RGP, de Korte CL. Noninvasive carotid strain imaging using angular compounding at large beam steered angles: validation in vessel phantoms. IEEE Trans Med Imag 2009;28(6):872–80.
[57] Hansen HHG, Lopata RGP, Idzenga T, de Korte CL. An angular compounding technique using displacement projection for noninvasive ultrasound strain imaging of vessel cross-sections. Ultrasound Med Biol 2010;36(11):1947–56.
[58] D'hooge J, Heimdal A, Jamal F, Kukulski T, Bijnens B, Rademakers F, et al. Regional strain and strain rate measurements by cardiac ultrasound: principles, implementation and limitations. Eur J Echocardiogr 2000;1(3):154–70.
[59] Yu CM, Fung JWH, Zhang Q, Chan CK, Chan YS, Lin H, et al. Tissue Doppler imaging is superior to strain rate imaging and postsystolic shortening on the prediction of reverse remodeling in both ischemic and nonischemic heart failure after cardiac resynchronization therapy. Circulation 2004;110(1):66–73.
[60] Heimdal A, Støylen A, Torp H, Skjærpe T. Real-time strain rate imaging of the left ventricle by ultrasound. J Am Soc Echocardiogr 1998;11(11):1013–9.
[61] Koyama J, Ray-Sequin PA, Falk RH. Longitudinal myocardial function assessed by tissue velocity, strain, and strain rate tissue Doppler echocardiography in patients with AL (primary) cardiac amyloidosis. Circulation 2003;107(19):2446–52.
[62] Greenberg NL, Firstenberg MS, Castro PL, Main M, Travaglini A, Odabashian JA, et al. Doppler-derived myocardial systolic strain rate is a strong index of left ventricular contractility. Circulation 2002;105(1):99–105.
[63] Edvardsen T, Gerber BL, Garot J, Bluemke DA, Lima JAC, Smiseth OA. Quantitative assessment of intrinsic regional myocardial deformation by Doppler strain rate echocardiography in humans. Circulation 2002;106(1):50–6.
[64] Jamal F, Strotmann J, Weidemann F, Kukulski T, D'hooge J, Bijnens B, et al. Noninvasive quantification of the contractile reserve of stunned myocardium by ultrasonic strain rate and strain. Circulation 2001;104(9):1059–65.
[65] Destrempes F, Meunier J, Giroux M-F, Soulez G, Cloutier G. Segmentation in ultrasonic B-mode images of healthy carotid arteries using mixtures of Nakagami distributions and stochastic optimization. IEEE Trans Med Imag 2009;28(2):215–29.
[66] Destrempes F, Meunier J, Giroux M-F, Soulez G, Cloutier G. Segmentation of plaques in sequences of ultrasonic B-mode images of carotid arteries based on motion estimation and a Bayesian model. IEEE Trans Biomed Eng 2011;58(8):2202–11.
[67] Dempster AP, Laird NM, Rubin DB. Maximum likelihood from incomplete data via the EM algorithm. J Roy Stat Soc Ser B (Methodological) 1977:1–38.
[68] Maurice RL, Bertrand M. Lagrangian speckle model and tissue-motion estimation-Theory. IEEE Trans Med Imag 1999;18(7):593–603.
[69] Maurice RL, Daronat M, Ohayon J, Stoyanova E, Foster FS, Cloutier G. Non-invasive high-frequency vascular ultrasound elastography. Phys Med Biol 2005;50(7):1611–28.
[70] Tobin MJ, Chadha TS, Jenouri G, Birch SJ, Gazeroglu HB, Sackner MA. Breathing patterns. 1. Normal subjects. Chest 1983;84(2):202–5.
[71] Lopata RGP, Nillesen MM, Hansen HHG, Gerrits IH, Thijssen JM, De Korte CL. Performance evaluation of methods for two-dimensional displacement and strain estimation using ultrasound radio frequency data. Ultrasound Med Biol 2009;35(5):796–812.
[72] Terrén EIC. Elastography: imaging of biological tissue elasticity. University of Houston; 1993.
[73] Kallel F, Ophir J. A least-squares strain estimator for elastography. Ultrason Imaging 1997;19:195–208.
[74] Giannattasio C, Failla M, Emanuelli G, Grappiolo A, Boffi L, Corsi D, et al. Local effects of atherosclerotic plaque on arterial distensibility. Hypertension 2001;38(5):1177–80.
[75] Bussy C, Boutouyrie P, Lacolley P, Challande P, Laurent S. Intrinsic stiffness of the carotid arterial wall material in essential hypertensives. Hypertension 2000;35(5):1049–54.
[76] Myers CW, Farquhar WB, Forman DE, Williams TD, Dierks DL, Taylor JA. Carotid distensibility characterized via the isometric exercise pressor response. Am J Physiol Heart Circ Physiol 2002;283(6):H2592–8.
[77] Kim K, Weitzel WF, Rubin JM, Xie H, Chen X, O'Donnell M. Vascular intramural strain imaging using arterial pressure equalization. Ultrasound Med Biol 2004;30(6):761–71.
[78] Dahl JJ, Dumont DM, Allen JD, Miller EM, Trahey GE. Acoustic radiation force impulse imaging for noninvasive characterization of carotid artery atherosclerotic plaques: a feasibility study. Ultrasound Med Biol 2009;35(5):707–16.
[79] Zhang H, Zhu T, Tian X, Zhou X, Li J, Wei Z, et al. Quantitative echocardiographic assessment of myocardial acceleration in normal left ventricle by using velocity vector imaging. J Am Soc Echocardiogr 2008;21(7):813–7.
[80] Jurcut R, Pappas CJ, Masci PG, Herbots L, Szulik M, Bogaert J, et al. Detection of regional myocardial dysfunction in patients with acute myocardial infarction using velocity vector imaging. J Am Soc Echocardiogr 2008;21(8):879–86.
[81] Nesser HJ, Winter S. Speckle tracking in the evaluation of left ventricular dyssynchrony. Echocardiography 2009;26(3):324–36.
[82] Wang Y, Chang C, Chen J, Hsiu H, Wang W. Pressure wave propagation in arteries. A model with radial dilatation for simulating the behavior of a real artery. IEEE Eng Med Biol Mag 1997;16(1):51–4.
[83] Pernot M, Fujikura K, Fung-Kee-Fung S, Konofagou E, et al. ECG-gated, mechanical and electromechanical wave imaging of cardiovascular tissues in vivo. Ultrasound Med Biol 2007;33(7):1075–85.
[84] Hansen HHG, Richards MS, Doyley MM, Korte CLd. Noninvasive vascular displacement estimation for relative elastic modulus reconstruction in transversal imaging planes. Sensors 2013;13(3):3341–57.